catalysts

MDPI

Article

Seeds Combining Pyrrolidine Control the Framework Al Distribution of FER Zeolite to Enhance Its Performance in the Skeletal Isomerization of *n*-Butene

Jinlong Fan [1,2], Xuedong Zhu [1,*], Fan Yang [1], Yarong Xu [2] and Lantian Chen [2]

[1] State Key Laboratory of Chemical Engineering, East China University of Science and Technology, Shanghai 200237, China; fanjlws@petrochina.com.cn (J.F.)
[2] Research Institute of Urumqi Petrochemical Company, Petrochina Co., Ltd., Urumqi 830019, China; xuyrws@petrochina.com.cn (Y.X.); chenltws@petrochina.com.cn (L.C.)
* Correspondence: xdzhu@ecust.edu.cn; Tel.: +86-21-64251005

Abstract: **FER** zeolites have a unique framework structure and acid distribution, and are widely studied as a catalyst for reactions such as *n*-butene skeletal isomerization and dimethyl ether carbonylation. The Brönsted acid site (BAS) located in the 10-member ring (10-MR) of **FER** zeolites serves as the active site for the isomerization reaction of skeletal *n*-butene to produce isobutene. This study prepared five types of **FER** zeolites using different methods: using pyrrolidine (PY) alone as a template; using Na-form **FER** as seeds (SN) or H-form **FER** as seeds without organic structure directing agents (OSDAs); and combining the seeds of SN or SH with PY as OSDAs. The differences in the structure and acid distribution of the five zeolites were investigated, as well as their catalytic performance for the skeletal isomerization of *n*-butene. Experiments and characterization results showed that under hydrothermal synthesis conditions, the FER-PY+SH zeolites synthesized by using both H-form zeolites seeds and pyridine exhibited the highest aluminum concentrations at T1 and T3 sites, along with the greatest BAS located in the 10-MR. This unique composition contributed to the highest selectivity of isobutene. The FER-PY+SH catalyst was continuously used for 720 h at 350 °C, 0.1 MPa, and an *n*-butene mass space velocity of 2.0 h^{-1} for three cycles of 2160 h. During this period, the conversion of *n*-butene was over 39%, while the selectivity of isobutene exceeded 95%. The FER-PY+SH catalyst exhibited excellent stability and activity.

Keywords: **FER** zeolites; seed; pyrrolidine; Al distribution; *n*-butene; skeletal isomerization

check for updates

Citation: Fan, J.; Zhu, X.; Yang, F.; Xu, Y.; Chen, L. Seeds Combining Pyrrolidine Control the Framework Al Distribution of FER Zeolite to Enhance Its Performance in the Skeletal Isomerization of *n*-Butene. *Catalysts* **2024**, *14*, 697. https://doi.org/10.3390/catal14100697

Academic Editor: Wladimir Reschetilowski

Received: 31 August 2024
Revised: 29 September 2024
Accepted: 3 October 2024
Published: 7 October 2024

Copyright: © 2024 by the authors. Licensee MDPI, Basel, Switzerland. This article is an open access article distributed under the terms and conditions of the Creative Commons Attribution (CC BY) license (https://creativecommons.org/licenses/by/4.0/).

1. Introduction

Isobutene is an important basic organic chemical raw material, which can be used to produce many high value-added products, including butyl rubber, polyisobutylene, methyl tert-butyl ether (MTBE), and methyl methacrylate. One of the primary industrial methods of production involves the skeletal isomerization of *n*-butene to generate isobutene [1–3]. In the past few decades, extensive research has focused on the production of isobutene through the skeleton isomerization of *n*-butene, utilizing various catalysts such as phosphoric acid, metal halides, aluminum oxide, phosphated and halogenated aluminum oxide, and zeolite molecular sieves [4,5]. The pore structure of **FER** zeolite includes two vertically intersecting two-dimensional pore systems: an 8-member ring (8-MR) pore (0.35 × 0.48 nm) along the [010] direction, a 10-member ring (10-MR) pore (0.43 × 0.55 nm) along the [001] direction, and a ferrierite cage with a diameter of approximately 0.6–0.7 nm formed by the intersection of a 6-member ring (6-MR) and 8-MR [6,7]. **FER** zeolite is currently the highest-performing *n*-butene skeleton isomerization catalyst and was successfully applied in industrial applications in the 1990s [8]. In the following decades, extensive research was conducted on the reaction mechanism of the skeletal isomerization of *n*-butene and on the synthesis and post-treatment modification of high-performance **FER** zeolites [9–11].

Numerous studies have demonstrated that the Brönsted acid site (BAS) located on the 10-MR in **FER** zeolite acts as a selective active site for catalyzing the skeleton isomerization of *n*-butene to produce isobutene. In contrast, the Lewis acid site (LAS) and BAS located on the 8-MR can exacerbate the occurrence of side reactions such as butene polymerization and cracking [12–16]. As is well known, zeolites are crystal compounds composed of TO4 (T atoms are generally Si or Al) tetrahedra according to certain rules. Their acidity mainly arises from the introduction of protons, which balance the negative charge of aluminum atoms in the framework of zeolites. It can be seen that the catalytic performance of zeolites is closely linked to the strength and position of acid sites. The strength and position of these acid sites are directly influenced by the distribution of Al atoms within the zeolite framework [17–20]. According to relevant information from the International Zeolite Association (IZA), the framework T atom of **FER** zeolites exhibits four distinct positions, namely the T1/T3 position, which can be connected to a 10-MR, and the T2/T4 position, which is solely connected through an 8-MR (note: labels of T atoms have been unified according to the **FER** framework in the IZA). Xiong et al. [21–23] used characterization methods such as MAS NMR and X-ray emission spectroscopy to study the distribution of framework aluminum atoms in **FER** zeolites. The results showed that **FER** zeolites induced by different organic structural directing agents (OSDAs) had different distributions of framework aluminum. Moreover, they combined MAS NMR spectroscopy and density functional theory to calculate the chemical shifts of aluminum located at positions T1/T2/T3/T4 in **FER** zeolites, which were 61, 51, 53, and 58 ppm, respectively.

In the synthesis process of zeolites, OSDAs play a crucial role in balancing the negative charge introduced by the aluminum atoms in the framework. Consequently, these OSDAs significantly influence the distribution of aluminum in zeolites. Pinar et al. [14,24,25] synthesized **FER** zeolites using a fluorinated system without the use of inorganic cations, using a combination of 1-benzoyl-1-methylpyrrolidinium, trimethylamine (TMA), pyridine, pyrrolidine (PY), and several organic template agents. The investigations indicate that **FER** zeolites induced by different organic structure directing agents have different skeletal aluminum distributions and exhibit different performances in *n*-butene skeletal isomerization reactions. Due to the different sizes of template molecules and their interactions with skeleton atoms, **FER** zeolites with different framework aluminum distributions can be obtained. When larger size OSDAs are used, a longer crystallization time is required to increase the distribution probability of aluminum atoms in the 10-MR, enhance the BAS of the 10-MR, and improve the control of the activity and selectivity of *n*-butene skeleton isomerization. Conversely, this tends to lead to side reactions such as butene polymerization and cracking, and accelerate catalyst deactivation. In addition, the studies of Leshkov [26] and Chu [27] also indicate that when different sizes of cyclic or chain amines are used as OSDAs, **FER** zeolites with different 10-MR and 8-MR aluminum distributions can also be obtained. Numerous studies have shown that the distribution of aluminum in the framework of zeolites is not only influenced by OSDAs, but also by the synthesis conditions of zeolites [28] and the selection of silicon and aluminum sources [29,30], solvents [31], inorganic cations [32–34], and post-treatment [35–37]. During the seed-induced synthesis of zeolites, the seed can play a role in reducing or avoiding the use of OSDAs, shortening crystallization time, avoiding impurities, and regulating the crystal morphology of target zeolites [38–40]. Xiao et al. [41] believe that due to the multiple roles of the seed in inducing the synthesis of zeolites, the seed can be regarded as the third type of structure directing agents, in addition to inorganic cations and OSDAs. Zhang et al. [42] synthesized **FER** zeolite with good crystallinity, large surface area, uniform micropores, and abundant acidic sites using RUB-37 as the crystal seed without OSDAs. Studies by Ham et al. [43–45] showed a change in the distribution of framework aluminum atoms in seed-induced synthesized **FER** zeolites as compared to **FER** zeolites as the seed. The higher BAS content of the 8-MR than the 10-MR resulted in better dimethyl ether carbonylation activity and stability of the seed-induced **FER** zeolites than the seed. In addition, Nishitoba [30] found that when using TMA as an OSDA to synthesize **CHA** zeolites, the addition of **FAU** zeolites

as crystal seeds and aluminum sources could regulate the distribution of aluminum atoms in the framework of **CHA** zeolites. These studies indicate that the distribution of aluminum in the zeolite framework can be modulated using the seed induction methods.

In this work, the synthesis of **FER** zeolites under different conditions was investigated as follows: using only pyrrolidine in OSDA synthesis; using only Na-form seed (SN)-induced synthesis; using only H-form seed (SH)-induced synthesis; and combining SN or SH + PY. The distribution of aluminum atoms in the framework of **FER** zeolites synthesized by different methods and their catalytic performance for *n*-butene skeleton isomerization reaction were investigated. The obtained catalyst of **FER** zeolites by inducing H-form seeds + PY as OSDAs has the highest distribution of 10-MR framework aluminum, which enhanced the acidic strength in the 10-MR and significantly improved the catalytic activity and selectivity of **FER** zeolites for the *n*-butene skeleton isomerization reaction. A new method for regulating the distribution of the framework of aluminum and acid in the **FER** zeolites was proposed.

2. Results and Discussion

2.1. Structural and Textural Properties

As shown in Figure 1, XRD patterns of FER-PY, FER-SN, FER-SH, FER-PY+SN, and FER-PY+SH exhibit typical diffraction peaks at 9.3°, 22.3°, 23.5°, 24.3°, 25.2°, 25.7°, and 28.5° out of the (200), (321), (330), (112), (040), (202), and (312) crystal planes in the **FER** topology (PDF #44-0104), respectively, indicating the successful formation of the **FER** zeolite without detectable impurities [22,23]. The relative crystallinity (RC) was calculated by integrating the areas of diffraction peaks within 9.3-28.5°, and the sum of the areas of FER-PY was set as 100% for reference. As listed in Table 1, the calculated RC values are comparable, measuring 101%, 99%, 100%, and 101% for FER-SN, FER-SH, FER-PY+SN, and FER-PY+SH, respectively. The above results indicate that several templates, such as PY, SN, SH, PY+SN, and PY+SH, can induce the synthesis of well-crystallized **FER** zeolites. The composition information is listed in Table 1, where the SiO_2 to Al_2O_3 ratios (SARs) of the five samples are within 24.6–25.6. Additionally, the Na_2O contents are all below 43 mg/g, suggesting that all FER-X samples have similar compositions and acidic densities. The calculated texture parameters are shown in Table 1; in line with the XRD observations, the specific surfaces and pore volumes remain relatively uniform, for instance, the values of S_{BET} average around 430 m^2/g, while V_{total} and V_{micro} are all about 0.27 cm^3/g and 0.14 cm^3/g, respectively.

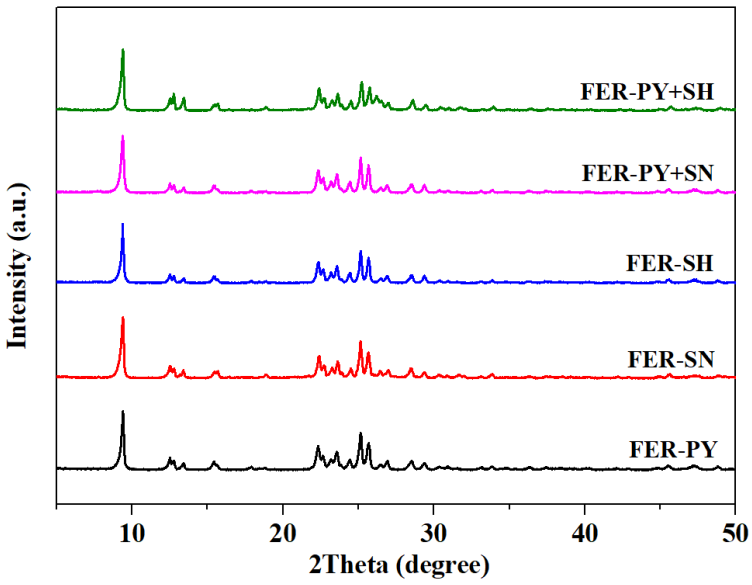

Figure 1. XRD patterns of various FER-X zeolites.

Table 1. Textural properties of various FER-X zeolites.

Sample	Na_2O (mg/g)	SARs	RC (%)	Surface Area (m^2/g)		Pore Volume (cm^3/g)	
				Total	Micro	Total	Micro
FER-PY	40	25.6	100	431	388	0.27	0.14
FER-SN	39	25.3	101	428	386	0.27	0.14
FER-SH	36	24.6	99	422	380	0.26	0.13
FER-PY+SN	42	25.3	100	430	378	0.28	0.14
FER-PY+SH	41	24.8	101	432	390	0.28	0.15

The SEM images (Figure 2) present the morphologies of the obtained FER-X zeolites. All samples are composed of hexagonal flake-like crystals with smooth surfaces; the average size of each flake is ~1 μm in length, ~500 nm in width, and 20~50 nm in thickness. Combined XRD and SEM analyses indicate that their morphology and structure are identical.

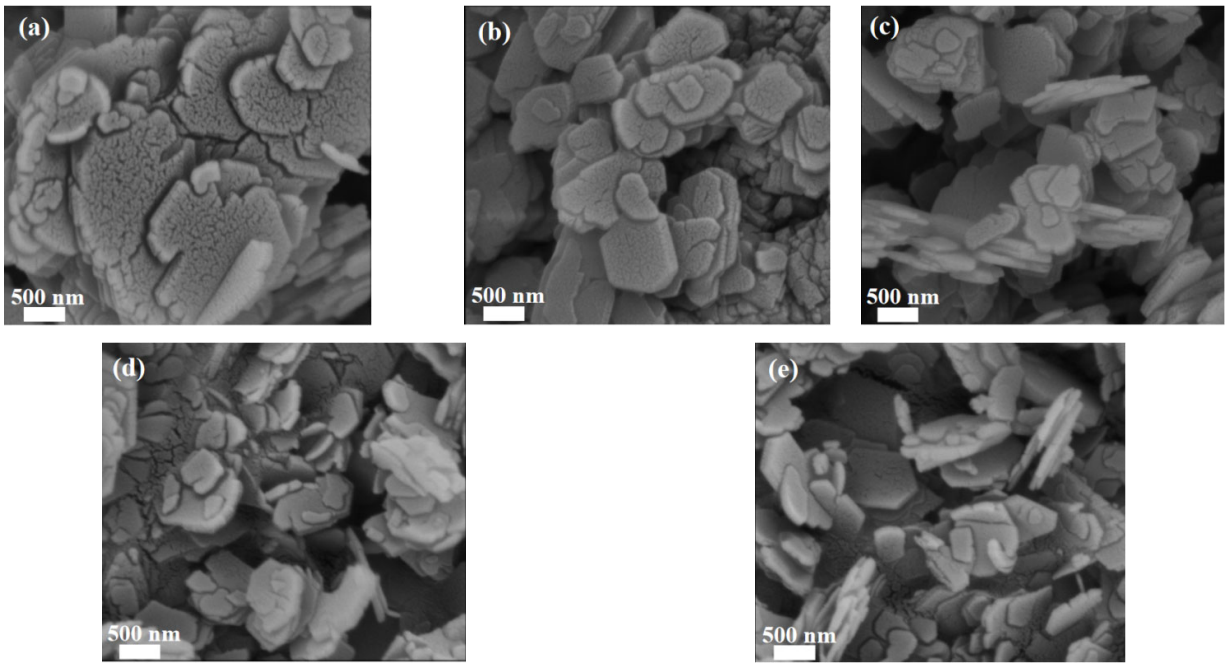

Figure 2. SEM images of various FER-X zeolites. (**a**) FER-PY, (**b**) FER-SN, (**c**) FER-SH, (**d**) FER-PY+SN, (**e**) FER-PY+SH.

2.2. Acidity Characterization

The acidic properties were characterized using NH_3-TPD and Py-IR. As illustrated in Figure 3, two NH_3 desorption peaks are observed at 195 °C and 450 °C (Figure 3a), corresponding to the desorption of NH_3 molecules that interact with the weak acids and strong acids, respectively. The positions of these peaks provide insight into acid strength, indicating that the weak and strong acid sites in FER-X samples exhibit similar acidic densities. Figure 3b–f shows the Py-IR spectrum was extracted at 150 °C, 250 °C, and 350 °C. The IR adsorption peak at 1450 cm^{-1} corresponds to the C-N stretching of pyridine adsorbed on LAS, while the peak at 1490 cm^{-1} is attributed to the C-H vibration of pyridine on both BAS and LAS. The peak at 1540 cm^{-1} is due to the N-H stretching of pyridinium cations generated by protonation of pyridine on BAS. As shown in Figure 3b–f, with the increase in desorption temperature, both BAS and LAS in the sample decrease. When the desorption temperature reaches 350 °C, LAS decreases to a very low level, indicating a

scarcity of strong LAS in the FER-X samples. In contrast, the decrease in BAS is considerably smaller, indicating a stronger acidity of BAS present in the FER-X samples.

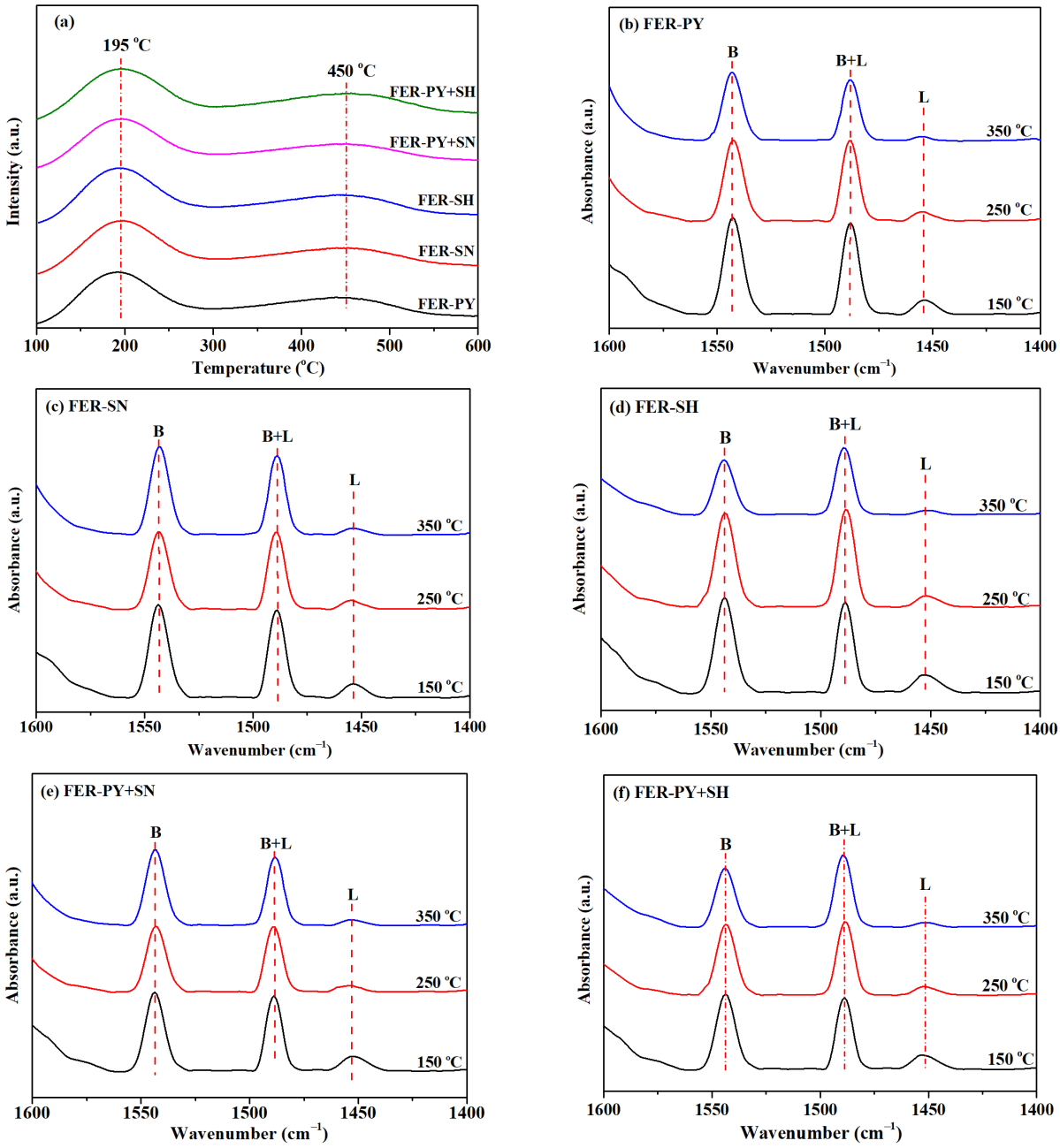

Figure 3. NH_3-TPD and Py-IR profiles of various FER-X zeolites. (**a**) NH_3-TPD profiles of FER-X zeolites, (**b**) Py-IR profiles of FER-PY, (**c**) Py-IR profiles of FER-SN, (**d**) Py-IR profiles of FER-SH, (**e**) Py-IR profiles of FER-PY+SN, (**f**) Py-IR profiles of FER-PY+SH.

The quantitative analysis of NH_3-TPD and Py-IR experiments is presented in Table 2. Notably, NH_3-TPD provides an overall assessment of the acidity of the samples, as the kinetic diameter of NH_3 (3.7 Å) is smaller than the 8-MR and 10-MR apertures in the **FER** structure. In contrast, Py-IR could only detect the acid sites located in 10-MR due to its larger kinetic diameter (5.7 Å for pyridine vs. 4.8 Å for 8-MR). Consequently, NH_3-TPD can be used to characterize the total acidity of FER-X zeolites, and Py-IR can be used to characterize the acidity of the 10-MR of FERX-zeolites (see the caption below Table 2 for more details). From the NH_3-TPD profiles, all samples have a similar acid

distribution and acid content, with acid densities around approximately 1.3 mmol/g for the five samples, consistent with their structural and compositional properties. However, more BAS can be identified over Py-IR for the FER-X samples (0.29 mmol/g for FER-PY and 0.28–0.34 mmol/g for others), especially for FER-PY+SH, whose value is 0.34 mmol/g. In addition, the BAS of desorption temperature as measured from Py-IR ($B_{10\text{-}350}$) is also shown in Table 2; this value is 0.20 mmol/g for FER-PY and increases monotonically to 0.32 mmol/g for FER-PY+SH. The differing acid distributions may arise from the distinct nucleation and crystal growth processes of zeolites synthesized using seed crystals, or a combination of seed crystals and organic templates, compared to those formed solely with organic templates. The different $B_{10\text{-}350}$ provides direct evidence that utilizing seeds or employing a combination of seeds and organic templates will alter the acid distribution in **FER** zeolite.

Table 2. Amounts of acid in the various FER-X samples.

Sample	Acidity by NH_3-TPD [a] (mmol/g)			Acidity by Py-IR [b] (mmol/g)			
	Weak	Strong	Total	Brønsted	Lewis	Total	$B_{10\text{-}350}$ [c]
FER-PY	0.79	0.56	1.35	0.29	0.03	0.32	0.20
FER-SN	0.78	0.55	1.33	0.28	0.03	0.31	0.24
FER-SH	0.75	0.53	1.28	0.28	0.03	0.31	0.25
FER-PY+SN	0.76	0.52	1.28	0.30	0.03	0.33	0.28
FER-PY+SH	0.81	0.56	1.37	0.34	0.02	0.35	0.32

[a] Acid sites on FER-X and their amounts were measured by NH_3-TPD analysis, and the quantities of weak and strong acid sites were calculated by using an integrated area at the maximum desorption temperatures of NH_3 at 195 °C and 450 °C, respectively. [b] Amounts of BAS and LAS were measured by Py-IR spectroscopy at a desorption temperature of 150 °C and 350 °C, and the number of acid sites was calculated using the well-known formula of BAS = $1.88A_BR^2/W$, LAS = $1.42A_LR^2/W$, where A_B and A_L are the integrated absorbance peak areas of BAS and LAS located at 1550 and 1450 cm^{-1}, respectively, R is the radius of a catalyst pellet of FER-X, cm, and W is the weight of catalyst, g [46]. [c] The number of BAS located in 10-MR at 350 °C was calculated by conducting Py-IR measurements at a desorption temperature of 350 °C.

2.3. *^{29}Si and ^{27}Al MAS NMR*

The ^{29}Si MAS NMR spectra show closely similar features (Figure 4), exhibiting four sub-peaks from the curve at approximately −100, −107, −112, and −116 ppm, respectively. The peaks at −100 and −107 ppm correspond to the Si atoms bonded to two Al atoms (Si(2Al)) and one Al atom (Si(1Al)), respectively, while the peaks at −112 and −116 ppm can be attributed to the Si atoms that are not adjacent any Al atoms (Si(0Al)), and silicon connecting to four Si tetrahedrons in the **FER** framework [21,47]. The weaker signal at −100 ppm of all samples indicates a lower prevalence of Al–O–Si–O–Al species on FER-X zeolites.

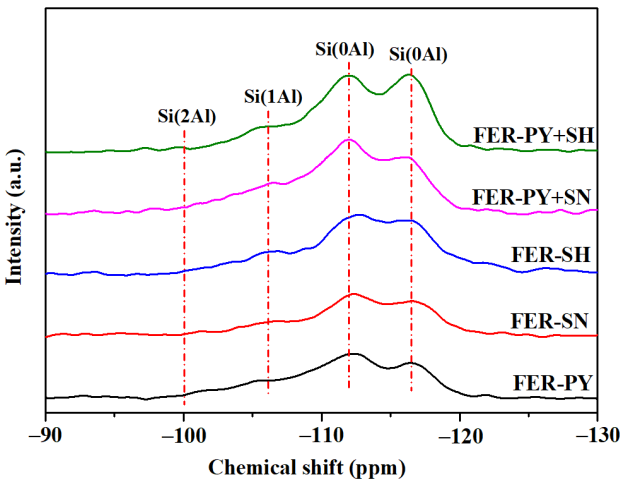

Figure 4. ^{29}Si MAS NMR spectra of various FER-X zeolites.

The ^{27}Al MAS NMR spectra of various FER-X zeolites are shown in Figure 5. As shown in Figure 5a, all of the FER-X samples exhibit a prominent resonance peak at 55 ppm corresponding to tetrahedrally coordinated Al species, while no signal peak appears at 0 ppm. This indicates that the aluminum atoms in zeolites samples are located on the framework of FER-X zeolites, and there is no non-framework aluminum present [42,43,48]. Previous studies have shown that aluminum atoms exhibit different NMR chemical shifts depending on their positions of T1, T2, T3, and T4 within the **FER** framework [21,23,47], and the ^{27}Al MAS NMR spectrum at 55 ppm is deconvolved into four peaks located at 61, 51, 53, and 58 ppm, respectively, as illustrated in Figure 5b–f. The Al population at T1–T4 sites in the FER-X samples was quantified from the corresponding ^{27}Al NMR spectra (Figure 5b–f) and Table 3. The FER-PY sample exhibited a minimal fraction of Al atoms on the T1 + T3 sites (30%). In comparison, the distribution proportion of aluminum on the T1 + T3 positions in FER-SN, FER-SH, and FER-PY+SN gradually increased to 41%, 44%, and 50% respectively, while the distribution proportion of aluminum at T1 + T3 positions on FER-PY+SN reached the highest value of 60%. Notably, each of the five samples contained a small amount of Al on the T1 site (0~12%).

Table 3. Aluminum distribution obtained from the curve fitting of ^{27}Al MAS NMR spectra of various FER-X zeolites.

Sample	Aluminum Distribution (%)				
	T1	T2	T3	T4	T1 + T3
FER-PY	0	30	30	39	30
FER-SN	8	19	33	40	41
FER-SH	10	25	34	31	44
FER-PY+SN	12	21	38	29	50
FER-PY+SH	6	15	54	25	60

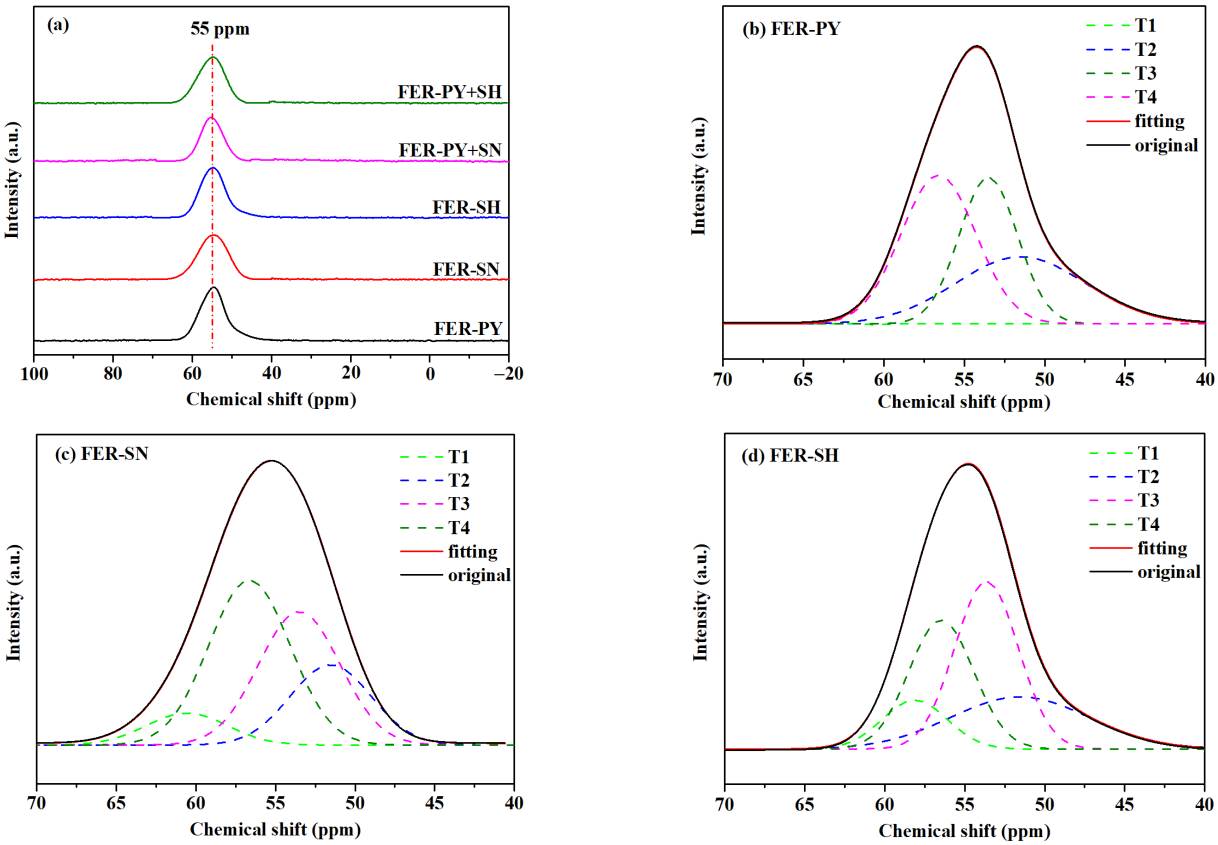

Figure 5. *Cont.*

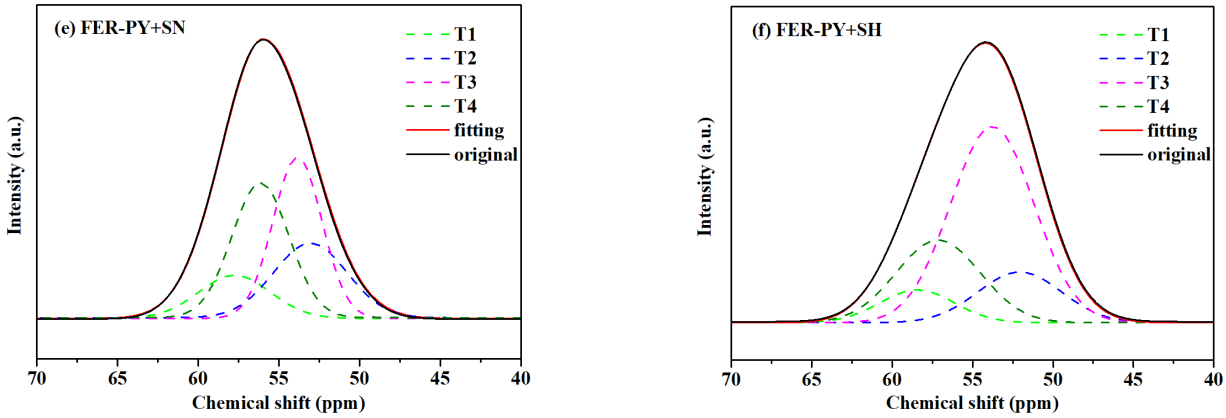

Figure 5. ^{27}Al MAS NMR spectra of various FER-X zeolites and Al distribution obtained from the curve deconvolved of FER-X zeolites. (**a**) ^{27}Al MAS NMR spectra of FER-X zeolites, (**b**) deconvolved of FER-PY, (**c**) deconvolved of FER-SN, (**d**) deconvolved of FER-SH, (**e**) deconvolved of FER-PY+SN, (**f**) deconvolved of FER-PY+SH.

In summary, using PY as an OSDA to induce the synthesis of FER-PY zeolites as a reference, all samples possessed similar compositional and textural properties, are total acid densities were closely aligned. Nevertheless, the combined use of pyrrolidine and H-form **FER** seeds renders a distinctive acid distribution, with a greater number of strong acid sites located in the 10-MR. To elucidate the relationship between the aluminum distribution and the acid distributions of FER-X zeolites, Figure 6 correlates the aluminum distribution data at T1 + T3 sites of different samples with $B_{10\text{-}350}$. A linear relationship can be observed between T1 + T3 and $B_{10\text{-}350}$, implying the acid distributions positively correlate with the quality of the aluminum distribution on T1 + T3. Several factors may contribute to this result. Firstly, the use of seed crystals to facilitate **FER** zeolite synthesis accelerates the nucleation and crystallization processes, potentially leading to a higher distribution of aluminum within the 10-MR. Secondly, the lower sodium content in H-form **FER** seeds allows for larger species to balance the framework charge, thereby increasing the likelihood of aluminum being positioned at T1 + T3 sites in the 10-MR. Moreover, this effect is more pronounced in the presence of PY as OSDAs alongside H-form **FER** seeds.

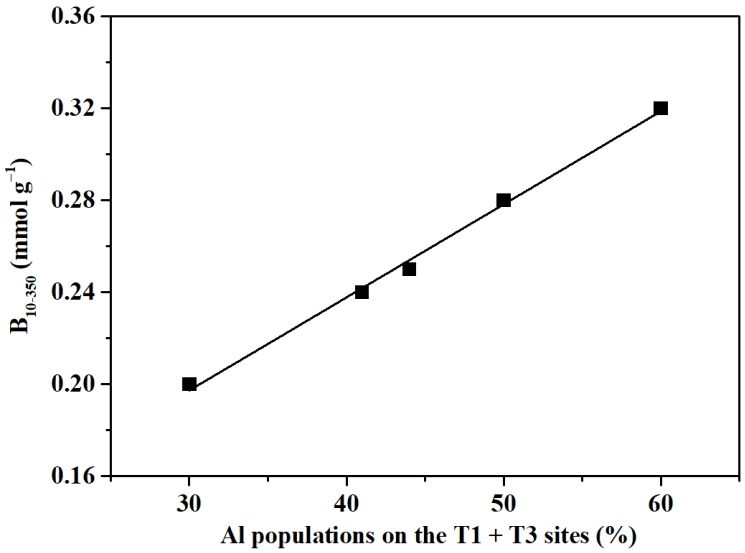

Figure 6. The influence of the Al populations on the T1 + T3 sites on the $B_{10\text{-}350}$ of various FER-X zeolites.

2.4. Catalytic Performance

The catalytic performances of all FER-X samples in *n*-butene skeletal isomerization are shown in Figure 7; the C4 hydrocarbons produced by fluidized catalytic cracking in refineries react with methanol to produce MTBE after removing isobutene (post-MTBE C4) and are used as feed.

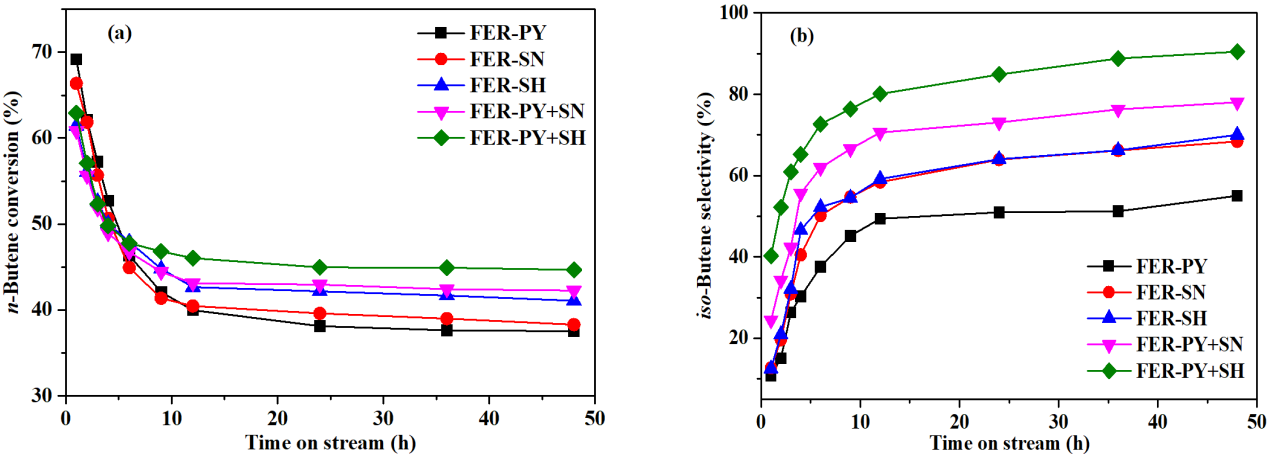

Figure 7. Catalytic performance of various FER-X zeolites for skeletal isomerization of *n*-butene with post-MTBE C4 as feed. (**a**) *n*-butene conversion of FER-X zeolites within time on stream, (**b**) *iso*-butene selectivity of FER-X zeolites within time on stream. Reaction conditions: T = 350 °C; p = 0.1 MPa; $WHSV_{n\text{-butene}}$ = 2.0 h^{-1}.

Figure 7a illustrates the relationship between the *n*-butene conversion and time on stream for FER-X catalyzed *n*-butene skeletal isomerization. As can be seen from the figure, FER-X catalysts exhibit the same trend, that is, with the extension of time on stream, the conversion initially decreases rapidly and then gradually stabilizes. Both FER-PY and FER-SN showed the best initial activities, achieving *n*-butene conversions exceeding 65%, while the initial conversions of the other samples fall within the range of 60% to 63%. This may be mainly due to the presence of more framework aluminum at the T2 + T4 sites in FER-PY and FER-SN, which resulted in more side reactions such as polymerization and cracking, leading to a higher conversion of *n*-butene. As the reaction proceeded, all conversions dropped rapidly during the first 12 h and then stabilized, by approximately 45% after running for 48 h.

In contrast, the selectivity of isobutene showed a completely reversed trend from that in Figure 7b. In the initial stage, the selectivity over FER-PY, FER-SN, and FER-SH was below 20%, while FER-PY+SN and FER-PY+SH recorded 25% and 40%, respectively. With the extension of time on stream, the selectivity over FER-PY gradually increased to ~55% after 48 h. FER-SN and FER-SH both presented a sharp increase in the first 12 h and then kept steady, with the selectivity reaching ~63% at 48 h. The selectivity over FER-PY+SN and FER-PY+SH also presented a sharp increase in the first 12 h, leveling off at about 78% and 90% after 48 h, respectively.

The experimental results in Figure 7 are mainly due to the different acid distributions of the FER-X catalysts. It is generally believed that the skeleton isomerization of *n*-butene to produce isobutene is carried out through the joint action of the monomolecular mechanism and the bimolecular mechanism. The BAS located in the 10-MR of **FER** zeolites is the active site for the selective produce of isobutene from *n*-butene [48–50]. In the monomolecular mechanism, *n*-butene is first adsorbed and protonated into a carbenium cation on the acid site, after which it undergoes skeleton isomerization and proton feedback to afford isobutene. The bimolecular mechanism mainly involves polymerization and isomerization to generate various long-chain carbocations, which subsequently crack to produce isobutene and by-products such as propylene. In the initial stage of this reaction, the strong acid

sites of **FER** zeolite were well retained, resulting in the predominance of the bimolecular mechanism, which was followed by cracking and the generation of by-products. After the initial stage, carbon deposition began to cover the non-selective acid sites, leading to a decrease in catalyst activity while suppressing undesired side reactions. Previous investigations have proved that the BAS in 10-MR of **FER** zeolites is accountable for the skeleton isomerization of *n*-butene, while BAS in the 8-MR and LAS can exacerbate side reactions such as polymerization and cracking, despite their higher activity [51,52]. Therefore, FER-PY+SH demonstrates improved selectivity and isobutene yields owing to its higher $B_{10\text{-}350}$ concentration. As shown in Figure 8, the yield of isobutene increases with the increase in $B_{10\text{-}350}$ and Al distribution on the T1 + T3.

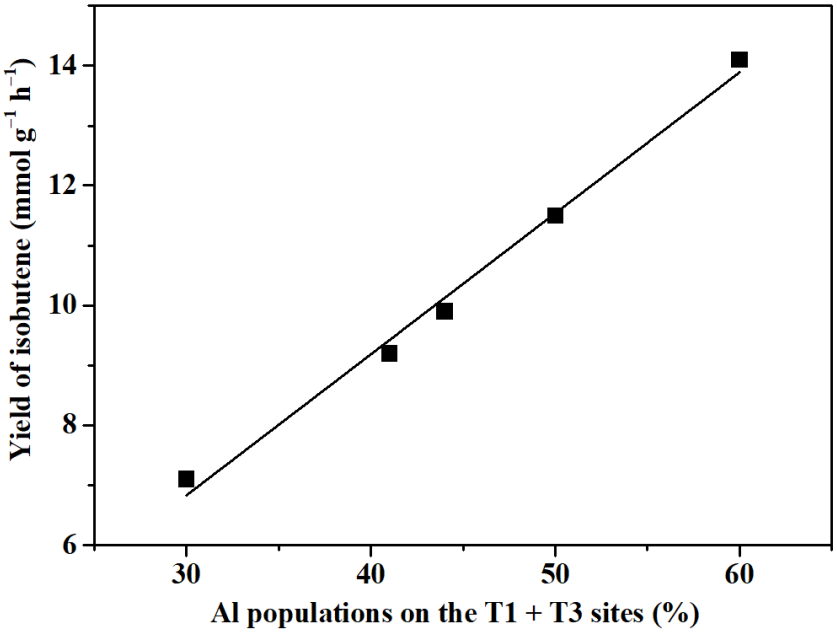

Figure 8. Relationship between yield of isobutene and Al populations on the T1 + T3 sites.

2.5. Catalyst Stability

Figure 9 displays the long-term stability tests using FER-PY+SH as candidate catalysts. The catalytic results were obtained with three cycles of regeneration (2160 h). The one-way life of the catalyst reaches 720 h, the conversion of *n*-butene (x_n) is greater than 39%, the selectivity of isobutene (s_i) is greater than 95%, and the yield of isobutene is greater than 37.5%. After 720 h of continuous reaction, the conversion of *n*-butene was below 39%, and catalyst regeneration was carried out at this time. After stopping the reaction, all deactivated catalysts were placed in a muffle furnace and the temperature was raised at a rate of 1 °C/min from 30 °C to 500 °C, and calcined at 500 °C for 12 h to complete the regeneration of the deactivated catalysts. Interestingly, after 720 h of one-way operation, the activity of FER-PY+SH in skeletal isomerization of *n*-butene was fully recovered after regeneration. This finding substantiates that FER-PY+SH can be effectively reused, thereby extending its lifespan beyond most reported catalysts in the skeletal isomerization of *n*-butene. The catalyst of FER-PY+SH exhibits superior catalytic activity due to its unique distribution of framework aluminum and enhanced acidic strength in the 10-MR.

In conclusion, the preparation of FER-PY+SH zeolites using a combination of H-form seeds and pyrrolidine enriches the number of BASs in the 10-MR, while improving the selectivity of isobutene and effectively suppressing the side reactions such as polymerization and cracking. The FER-PY+SH samples thus demonstrate excellent isobutene selectivity and yields in the skeletal isomerization of *n*-butene.

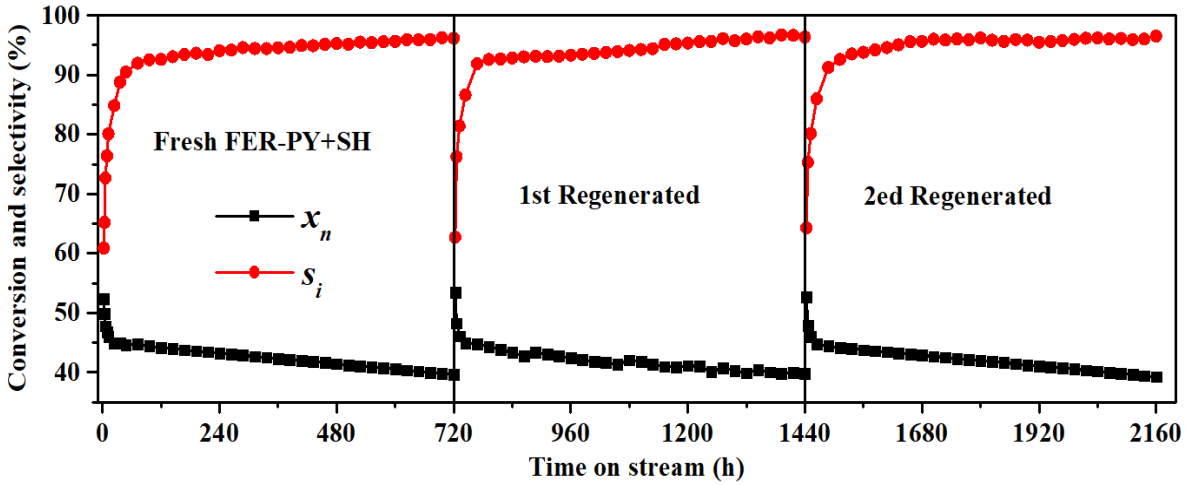

Figure 9. Stability of FER-PY+SH for skeletal isomerization of *n*-butene. Reaction conditions: T = 350 °C; p = 0.1 MPa; $WHSV_{n\text{-butene}}$ = 2.0 h^{-1}.

3. Experimental

3.1. Materials

The reagents used for the synthesis of **FER** zeolite were silica sol (SS3015, 30% SiO_2, 0.02%NaO_2, Shandong Baite New Material Co., Ltd. Linyi, Shandong, China), sodium metaaluminate ($NaAlO_2$, 99.0%, Tianjin Kermel Chemical Reagent Co., Ltd. Tianjin, China), sodium hydroxide (NaOH, 96.0%, Tianjin Kermel Chemical Reagent Co., Ltd. Tianjin, China), pyrrolidine (PY) (C_4H_9N, 99%, Tianjin Kermel Chemical Reagent Co., Ltd. Tianjin, China), ammonium chloride (NH_4Cl, 99%, Tianjin Kermel Chemical Reagent Co., Ltd. Tianjin, China), and deionized water.

3.2. Preparation of FER-X Zeolites

3.2.1. Preparation of Seeds

Typically, deionized water and NaOH aqueous solution were slowly added to silica sol (SiO_2, 30 wt%), and stirred vigorously for 1 h. Then, $NaAlO_2$ aqueous solution and PY were added, followed by stirring for 2 h to form a homogeneous suspension with a molar composition of 0.1 Na_2O:0.033 Al_2O_3:1 SiO_2:25 H_2O:0.22 PY. The suspension was transferred into a Teflon-lined stainless-steel autoclave and crystallized at 160 °C under a rotation of 200 rpm for 72 h. After the hydrothermal synthesis, the product was washed with distilled water until it reached a neutral pH. It was then dried at 120 °C overnight and calcinated at 550 °C in air for 6 h to obtain Na-form **FER**. The Na-form **FER** zeolites were subsequently converted into NH_4-form via ion exchange with 1 mol/L NH_4Cl solution at 80 °C for 2 h; this process was repeated twice. Then, the resulting white slurry was filtered and dried at 120 °C for 6 h. Finally, H-form **FER** zeolite catalysts were obtained by calcination of NH_4-form **FER** zeolites in air at 500 °C for 4 h. These Na-form **FER** and H-form **FER** were used as the seeds, and the seeds' abbreviations are SN and SH respectively.

3.2.2. Preparation of Seed-Derived FER-X Zeolites

The seed-derived **FER** zeolites were prepared as fellows: organic structure directing agents were not used, while the remaining synthetic processes were kept identical to the procedures described above. Finally, the SN and SH were added to form a homogeneous suspension with a molar composition of 0.1 Na_2O:0.033 Al_2O_3:1 SiO_2:25 H_2O: 15% wt seeds. The prepared mother gel was transferred into a Teflon-lined stainless-steel autoclave and crystallized at 160 °C under a rotation of 200 rpm for 72 h, followed by centrifuging, rinsing, and drying overnight at 120 °C to afford Na-form **FER**.

The method of synthesizing **FER** zeolites using both PY and SN or SH as seeds simultaneously is similar to the synthesis methods of the two aforementioned **FER** zeolites. Finally, the homogeneous suspension with a molar composition of 0.1 Na_2O:0.033 Al_2O_3:1 SiO_2:25 H_2O: 0.12 PY:15% wt SN or SH was transferred into a Teflon-lined stainless-steel reactor, and then hydrothermal synthesis was conducted for 72 h at 160 °C with 200 rpm. The white gel was obtained after several washing steps and dried at 120 °C for 6 h, and further calcined at 550 °C in air for 6 h to afford Na-form **FER**.

3.2.3. Preparation of H-form **FER** Zeolites

All of the Na-form **FER** zeolites were transformed into NH_4-form via ion exchange with 1 mol/L NH_4Cl solution at 80 °C for 2 h. This process was repeated twice. Then, the resulting white slurry was filtered and dried at 120 °C for 6 h. Finally, H-form **FER** zeolite catalysts were obtained by calcining of NH_4-form **FER** zeolites in air at 500 °C for 4 h. The H-form **FER** zeolite prepared using PY was labeled as FER-PY, the H-form **FER** zeolite prepared by Na-form **FER** zeolites as seeds induction was denoted as FER-SN, the H-form **FER** zeolite prepared by H-form **FER** zeolites as seeds induction was denoted as FER-SH, and the H-form **FER** zeolite prepared with PY and Na-form **FER** zeolites or H-form **FER** zeolites as seeds simultaneously was denoted as FER-PY+SN and FER-PY+SH, respectively. Finally, the H-form **FER** zeolite was compressed and formed to obtain a catalyst for the skeletal isomerization of *n*-butene.

3.3. Characterization of Catalysts

X-ray diffraction (XRD) was used to measure the crystallization and phase of the **FER** catalysts performed with a Rigaku D/max 2550 VB/PC diffractometer apparatus with Cu Ka radiation (λ = 0.15406 nm) at a voltage and current of 40 kV and 40 mA, respectively. The 2θ scanning range was from 5° to 40° with a scan rate of 4°/min and the step size of 0.02°. The R.C.s of the catalysts were obtained by calculating the sum of the peak intensity at $2\theta = 9.3 \pm 0.1°$, $22.3 \pm 0.1°$, $23.5 \pm 0.1°$, $24.3 \pm 0.1°$, $25.2 \pm 0.1°$, $25.7 \pm 0.1°$, and $28.5 \pm 0.1°$, and the R.C.s of FER-PY was set as 100%.

The scanning electron microscopy (SEM) images of the samples were analyzed using a Nava Nano SEM 450 microscope to confirm the crystal morphology and size. The sodium content and SiO_2/Al_2O_3 molar ratio of the samples were determined by X-ray fluorescence (XRF) analysis using a ZSX Primus II instrument (Rigaku, Tokyo, Japan) operated at 60 kV and 150 mA. The textural characterization of the **FER** catalysts was performed by N_2 adsorption–desorption at −196 °C with a US Micromeritics ASAP 2020 V3.00 H nitrogen adsorption analyzer (Atlanta, GA, USA). The **FER** catalysts were outgassed at 350 °C for 5 h under the vacuum of 10^{-3} Pa to remove moisture and volatile impurities before the adsorption measurement. The specific surface areas were obtained by the Brunauer–Emmett–Teller (BET) method and the pore volume was calculated by N_2 adsorption at a relative pressure of 0.99.

The temperature-programmed desorption of ammonium (NH_3-TPD) with a Micromeritics chemisorb 2720 (Atlanta, GA, USA) instrument equipped with a thermal conductivity detector was used to study the acid properties of the catalysts. Typically, 150 mg of the sample was first preheated under a He stream of 30 mL·min^{-1} at 550 °C for 1 h, then purged in a 5% NH_3-He flow of 30 mL/min at 100 °C for 40 min. Subsequently, the sample was treated under a He flow of 30 mL/min at 100 °C for 60 min to remove the physically adsorbed NH_3. Finally, the samples were heated from 100 °C to 550 °C using a temperature ramp of 10 °C/min, and the quantity of NH_3 desorbed was measured by a TCD detector.

Pyridine adsorption Fourier transform infrared (Py-IR) was used to determine B acid and L acid concentrations using a Bruker Tensor 27 infrared spectrometer. Approximately, the sample powder (30 mg) was formed into a self-supporting wafer (dimeter 20mm) and then placed inside the reaction tank. The sample was degassed under vacuum at 500 °C for 2 h under high vacuum conditions of 10^{-3} Pa, and then the sample was saturated with the

probe molecule pyridine at 40 °C for 30 min, and subsequently, the physisorbed molecules were removed at 150 °C for 30 min. IR spectra were recorded at 350 °C. The adsorption peaks located at 1540 cm^{-1} and 1450 cm^{-1} were assigned to BAS and LAS, respectively. The concentration of acid sites was calculated from the IR results using the extinction coefficient and integrated intensity of the desorption peak and the sample weight reported by Emeis [46].

Magic-angle-spinning nuclear-magnetic-resonance (MAS NMR) spectra of ^{27}Al and ^{29}Si were collected on a Bruker Avance III 600 MHz Wide Bore spectrometer (Bruker, Rheinstetten, Germany). The single-pulse sequence was adopted with a 10° pulse and a delay time of 0.3 s. The chemical shifts for ^{27}Al and ^{29}Si were calibrated by referring to $AlCl_3$ and tetramethylsilane, respectively. The ^{27}Al MAS NMR spectra were deconvoluted using the mixed Gaussian–Lorentzian equation.

3.4. Catalyst Evaluation

The skeletal isomerization of *n*-butene was conducted under atmospheric pressure in a fixed-bed stainless-steel reactor unit, with the tubular reactor having 12 mm inner diameter and 800 mm length. Firstly, 3 g of the FER-X catalyst (20–40 mesh) was placed in the middle of reactor, the catalyst was pretreated under a N_2 flow at a heating rate of 10 °C/min, and the system was purged for 1 h. The C4 hydrocarbons produced by fluidized catalytic cracking in refineries react with methanol to produce MTBE after removing isobutene (post-MTBE C4) and were used as reaction materials. The feed stream of post-MTBE C4 was fed into the reactor by a mass flow controller to start the skeletal isomerization; when heated to 350 °C, the weight hourly space velocity (WHSV) of *n*-butene was 2.0 h^{-1}. The properties of the post-MTBE C4 are listed in Table 4.

Table 4. Composition of post-MTBE C4 from refinery.

Composition	wt/%
propane	0.12
propylene	0.15
isobutane	52.86
butane	10.94
trans-2-butene	13.76
1-butene	12.00
isobutene	0.26
cis-2-butene	9.91

The products were analyzed using an Agilent 7890B gas chromatograph (Santa Clara, CA, USA) equipped with a flame ionization detector and an Agilent-GS-Alumina capillary column (50 m × 0.532 mm). Since the equilibrium of 1-butene, *trans*-2-butene, and *cis*-2-butene was established rapidly through double-bond isomerization at the temperature of the reaction, and all the straight-chain butene isomers were transformed to isobutylene, all of the straight-chain butene was considered as the *n*-butene reactant.

The conversion of *n*-butene (x_n) was defined as:

$$x_n = \frac{m_0 - m_1}{m_0} \times 100\% \quad (1)$$

The selectivity of isobutene (s_i) was defined as:

$$s_i = \frac{m_2 - m_3}{m_0 - m_1} \times 100\% \quad (2)$$

where m_0, m_1, m_2, and m_3 are the weights of *n*-butene in the feed, the weights of *n*-butene in the products, the weights of isobutene in the reaction products, and the weights of isobutene in the feed, respectively.

The production rate of isobutene was defined as the average moles of isobutene produced at the reaction duration of 24–48 h [mmol g^{-1} h^{-1}].

4. Conclusions

FER-type zeolites have been successfully prepared in pyrrolidine as an organic template or without pyrrolidine systems utilizing the Na-form or H-form as the seed. The seed-derived **FER** samples own similar topological and morphological properties compared to the pyrrolidine-derived sample, as well as similar total acid densities. The choice of the H-form seed and pyrrolidine induces more BAS in the 10-MR of the **FER** structure. As the BAS in 8-MR and LAS is responsible for the bimolecular mechanism that tends to cause more carbon depositions and side-products in *n*-butene skeleton isomerization, the FER-PY+SH samples exhibit better isobutene selectivity and higher stability than the counterparts synthesized by Na-form as the normal seed. By optimizing the synthetic parameters, FER-PY+SH could be continuously operated for 720 h at 350 °C and 0.1 MPa for three cycles, and a weight hourly space velocity of *n*-butene of 2.0 h^{-1}, during which the *n*-butene conversion keeps higher than 39%, the selectivity of isobutene is higher 95%, and the isobutene yield is higher than 37.5%.

Author Contributions: J.F.: investigation, data curation, writing—original draft. X.Z.: methodology, conceptualization, supervision, writing—review and editing. F.Y.: methodology, writing—original draft. Y.X.: methodology formal analysis, project administration. L.C.: validation, formal analysis. All authors have read and agreed to the published version of the manuscript.

Funding: This research received the funding of the project by CNPC (2018B-1907).

Data Availability Statement: Data are contained within the article.

Conflicts of Interest: Author Jinlong Fan, Yarong Xu and Lantian Chen were employed by the company of Research Institute of Urumqi Petrochemical Company, Petrochina Company Limited. The remaining authors declare that the research was conducted in the absence of any commercial or financial relationships that could be construed as a potential conflict of interest.

Abbreviations

Content	Abbreviations
Brönsted acid sites	BAS
10-member ring	10-MR
pyrrolidine	PY
Na-form **FER** as seeds	SN
H-form **FER** as seeds	SH
organic structure directing agents	OSDAs
8-member ring	8-MR
6-member ring	6-MR
International Zeolite Association	IZA
methyl tert-butyl ether	MTBE
trimethylamine	TMA
relative crystallinity	RC
SiO_2 to Al_2O_3 ratios	SARs
BAS of desorption temperature as measured from Py-IR	$B_{10\text{-}350}$
C4 hydrocarbons produced by fluidized catalytic cracking in refineries react with methanol to produce MTBE after removing isobutene	post-MTBE C4
weight hourly space velocity	WHSV

References

1. Díaz Velázquez, H.; Likhanova, N.; Aljammal, N.; Verpoort, F.; Martínez-Palou, R. New Insights into the Progress on the Isobutane/Butene Alkylation Reaction and Related Processes for High-Quality Fuel Production. A Critical Review. *Energy Fuels* **2020**, *34*, 15525–15556. [CrossRef]
2. Xu, Q.; Yang, W.; Chen, Z.; Ye, Y.; Luo, Y.; Street, J.; Zhou, H.; Xu, C. Formation and regeneration of shape-selective ZSM-35 catalysts for n-Butene skeletal isomerization to isobutylene. *ACS Omega* **2018**, *3*, 8202–8211. [CrossRef] [PubMed]

3. Corma, A. Inorganic solid acids and their use in acid-catalyzed hydrocarbon reactions. *Chem. Rev.* **1995**, *95*, 559–614. [CrossRef]
4. Houzvicka, J.; Ponec, V. Skeletal isomerization of n -Butenes. *Catal. Reviews. Sci. Eng.* **1997**, *39*, 319–344. [CrossRef]
5. Paul, M.; Naccache, C. Skeletal isomerisation of n-butenes catalyzed by medium-pore zeolites and aluminophosphates. *Adv. Catal.* **2010**, *31*, 505–543.
6. Vaughan, P.A. The crystal structure of the zeolite ferrierite. *Acta Crystallogr.* **1966**, *21*, 983–990. [CrossRef]
7. Xu, H.; Zhu, J.; Zhu, L.; Zhou, E.; Shen, C. Advances in the synthesis of ferrierite zeolite. *Molecules* **2020**, *25*, 3722. [CrossRef]
8. Mooiweer, H.H.; de Jong, K.P.; Kraushaar-Czarnetzki, B.; Stork WH, J.; Krutzen BC, H. Skeletal isomerisation of olefins with the zeolite ferrierite as catalyst. *Stud. Surf. Sci. Catal.* **1994**, *84*, 2327–2334.
9. Guo, G.Q.; Long, Y.C. Advances in the catalysis of skeletal isomerization of n-butene into iso-butene on FER zeolite. *Chem. Ind. Eng. Prog.* **2006**, *6*, 16–19.
10. Liu, W.; Hu, H.; Liu, Y.; Zhang, L.; Xia, C.; Wang, Q.; Ke, M. Distribution of effective ferrierite active sites for skeletal isomerization of n-butene to isobutene. *ChemistrySelect* **2019**, *4*, 7851–7857. [CrossRef]
11. Wang, Y.; Gao, Y.; Chu, W.; Zhao, D.; Chen, F.; Zhu, X.; Li, X.; Liu, S.; Xie, S.; Xu, L. Synthesis and catalytic application of FER zeolites with controllable size. *J. Mater. Chem. A* **2019**, *7*, 7573–7580. [CrossRef]
12. Wichterlová, B.; Žilkova, N.; Uvarova, E.; Čejka, J.; Sarv, P.; Paganini, C.; Lercher, J.A. Effect of Broensted and Lewis sites in ferrierites on skeletal isomerization of n-Butenes. *Appl. Catal. A Gen.* **1999**, *182*, 297–308. [CrossRef]
13. Domokos, L.; Lefferts, L.; Seshan, K.; Lercher, J. The importance of acid site locations for n-Butene skeletal isomerization on ferrierite. *J. Mol. Catal. A Chem.* **2000**, *162*, 147–157. [CrossRef]
14. Pinar, A.; Márquez-Álvarez, C.; Grande-Casas, M.; Pérez-Pariente, J. Template-controlled acidity and catalytic activity of ferrierite crystals. *J. Catal.* **2009**, *263*, 258–265. [CrossRef]
15. Seo, G.; Jeong, H.S.; Hong, S.B.; Uh, Y.S. Skeletal isomerization of 1-Butene over ferrierite and ZSM-5 zeolites: Influence of zeolite acidity. *Catal. Lett.* **1996**, *36*, 249–253. [CrossRef]
16. Van Donk, S.; Bus, E.; Broersma, A.; Bitter, J.H.; de Jong, K.P. Probing the accessible sites for n-Butene skeletal isomerization over aged and selective H-Ferrierite with d3-acetonitrile. *J. Catal.* **2002**, *212*, 86–93. [CrossRef]
17. Corma, A. From Microporous to Mesoporous Molecular Sieve Materials and Their Use in Catalysis. *Chem. Rev.* **1997**, *97*, 2373–2420. [CrossRef]
18. Li, J.; Gao, M.; Yan, W.; Yu, J. Regulation of the Si/Al ratios and Al distributions of zeolites and their impact on properties. *Chem. Sci.* **2023**, *14*, 1935–1959. [CrossRef]
19. Mercedes, B.; Corma, A. What Is Measured When Measuring Acidity in Zeolites with Probe Molecules? *ACS Catal.* **2019**, *9*, 1539–1548.
20. Palčić, A.; Valtchev, V. Analysis and control of acid sites in zeolites. *Appl. Catal. A Gen. Int. J. Devoted Catal. Sci. Its Appl.* **2020**, *606*, 117795. [CrossRef]
21. Xiong, Z.; Qi, G.; Bai, L.; Zhan, E.; Chu, Y.; Xu, J.; Ta, N.; Hao, A.; Deng, F.; Shen, W. Preferential population of Al atoms at the T4 site of ZSM-35 for the carbonylation of dimethylether. *Catal. Sci. Technol.* **2022**, *12*, 4993–4997. [CrossRef]
22. Bohinc, R.; Hoszowska, J.; Dousse, J.-C.; Błachucki, W.; Zeeshan, F.; Kayser, Y.; Nachtegaal, M.; Pinar, A.B.; van Bokhoven, J.A. Distribution of aluminum over different T-sites in ferrierite zeolites studied with aluminum valence to core X-ray emission spectroscopy. *Phys. Chem. Chem. Phys.* **2017**, *19*, 29271–29277. [CrossRef] [PubMed]
23. Pinar, A.B.; Verel, R.; Pérez-Pariente, J.; van Bokhoven, J.A. Direct evidence of the effect of synthesis conditions on aluminum sitting in zeolite ferrierite: A ^{27}Al MQ MAS NMR study. *Microporous Mesoporous Mater.* **2014**, *193*, 111–114. [CrossRef]
24. Pinar, A.B.; Gómez-Hortigüela, L.; McCusker, L.B.; Pérez-Pariente, J. Controlling the Aluminum Distribution in the Zeolite Ferrierite via the Organic Structure Directing Agent. *Chem. Mater.* **2013**, *25*, 3654–3661. [CrossRef]
25. Márquez-Alvarez, C.; Pinar, A.B.; García, R.; Grande-Casas, M.; Pérez-Pariente, J. Influence of Al distribution and defects concentration of ferrierite catalysts synthesised from na-free gels in the skeletal isomerisation of n-Butene. *Top. Catal.* **2009**, *52*, 1281–1291. [CrossRef]
26. Román-Leshkov, Y.; Moliner, M.; Davis, M.E. Impact of Controlling the Site Distribution of Al Atoms on Catalytic Properties in Ferrierite-Type Zeolites. *J. Phys. Chem. C* **2011**, *115*, 1096–1102. [CrossRef]
27. Chu, W.; Liu, X.; Yang, Z.; Nakata, H.; Tan, X.; Liu, X.; Xu, L.; Guo, P.; Li, X.; Zhu, X. Constrained Al sites in FER-type zeolites. *Chin. J. Catal.* **2021**, *42*, 2078–2087. [CrossRef]
28. Kim, S.; Park, G.; Woo, M.H.; Kwak, G.; Kim, S.K. Control of hierarchical structure and framework-Al distribution of ZSM-5 via adjusting crystallization temperature and their effects on methanol conversion. *ACS Catal.* **2019**, *9*, 2880–2892. [CrossRef]
29. Gábová, V.; Dědeček, J.; Čejka, J. Control of Al distribution in ZSM-5 by conditions of zeolite synthesis. *J. Chem. Commun.* **2003**, *10*, 1196–1197. [CrossRef]
30. Nishitoba, T.; Yoshida, N.; Kondo, J.N.; Yokoi, T. Control of Al distribution in the CHA-type aluminosilicate zeolites and its impact on the hydrothermal stability and catalytic properties. *Ind. Eng. Chem. Res* **2018**, *57*, 3914–3922. [CrossRef]
31. Heard, C.J.; Grajciar, L.; Nachtigall, P. The effect of water on the validity of Lwenstein's rule. *Chem. Sci.* **2019**, *10*, 5705–5711. [CrossRef] [PubMed]
32. Di Iorio, J.R.; Gounder, R. Controlling the isolation and pairing of aluminum in Chabazite zeolites using mixtures of organic and inorganic structure-directing agents. *Chem. Mater.* **2016**, *28*, 2236–2247. [CrossRef]

33. Di Iorio, J.R.; Li, S.; Jones, C.B.; Nimlos, C.T.; Wang, Y.; Kunkes, E.; Vattipalli, V.; Prasad, S.; Moini, A.; Schneider, W.F.; et al. Cooperative and competitive occlusion of organic and inorganic structure directing agents within Chabazite zeolites influences their aluminum arrangement. *J. Am. Chem. Soc.* **2020**, *142*, 4807–4819. [CrossRef]
34. Fletcher, R.E.; Ling, S.; Slater, B. Violations of Löwensteins rule in zeolites. *Chem Sci* **2017**, *8*, 7483–7491. [CrossRef]
35. Inagaki, S.; Yamada, N.; Nishii, M.; Nishi, Y.; Kubota, Y. Control of framework Al distribution in ZSM-5 zeolite via post-synthetic $TiCl_4$ treatment. *Microporous Mesoporous Mater.* **2020**, *302*, 1102231–1102239. [CrossRef]
36. Vjunov, A.; Fulton, J.L.; Huthwelker, T.; Pin, S.; Mei, D.; Schenter, G.K.; Govind, N.; Camaioni, D.M.; Hu, J.Z.; Lercher, J.A. Quantitatively Probing the Al Distribution in Zeolites. *Am. Chem. Soc.* **2014**, *136*, 8296–8306. [CrossRef]
37. Holzinger, J.; Beato, P.; Lundegaard, L.F.; Skibsted, J. Distribution of Aluminum over the tetrahedral sites in ZSM-5 zeolites and their evolution after steam treatment. *J. Phys.Chem. C Nanomater. Interfaces* **2018**, *122*, 15595–15613. [CrossRef]
38. Meng, X.J.; Xiao, F.S. Green routes for synthesis of zeolites. *Chem. Reviews.* **2014**, *114*, 1521–1543. [CrossRef]
39. Ye, Z.; Zhang, H.; Zhang, Y.; Tang, Y. Seed-induced synthesis of functional MFI zeolite materials: Method development, crystallization mechanisms, and catalytic properties. *Front. Chem. Sci. Eng.* **2020**, *14*, 143–158. [CrossRef]
40. Zhang, H.; Zhao, Y.; Zhang, H.; Wang, P.; Shi, Z.; Mao, J.; Zhang, Y.; Tang, Y. Tailoring zeolite ZSM-5 crystal morphology porosity through flexible utilization of Silicalite-1 seeds as templates: Unusual crystallization pathways in a heterogeneous system. *Chem. A Eur. J.* **2016**, *22*, 7141–7151. [CrossRef]
41. Ji, Y.; Wang, Y.; Xie, B.; Xiao, F.S. Zeolite Seeds: Third Type of Structure Directing Agents in the Synthesis of Zeolites. *Comments Inorg. Chem.* **2016**, *36*, 1–16. [CrossRef]
42. Zhang, H.; Guo, Q.; Ren, L.; Yang, C.; Zhu, L.; Meng, X.; Li, C.; Xiao, F.-S. Organotemplate-free synthesis of high-silica ferrierite zeolite induced by CDO-structure zeolite building units. *J. Mater. Chem.* **2011**, *21*, 9494–9497. [CrossRef]
43. Ham, H.; Jung, H.S.; Kim, H.S.; Kim, J.; Cho, S.J.; Lee, W.B.; Park, M.J.; Bae, J.W. Gas-phase carbonylation of dimethyl ether on the stable seed derived Ferrierite. *ACS Catal* **2020**, *10*, 5135–5146. [CrossRef]
44. Kim, J.; Ham, H.; Jung, H.S.; Wang, Y.; He, Y.; Tsubaki, N.; Cho, S.J.; Han, G.Y.; Bae, J.W. Dimethyl ether carbonylation to methyl acetate over highly crystalline zeolite-seed derived Ferrierite. *Catal. Sci. Technol.* **2018**, *8*, 3060–3072. [CrossRef]
45. Kwak, S.J.; Kim, H.S.; Park, N.; Park, M.J.; Lee, W.B. Recent progress on Al distribution over zeolite frameworks: Linking theories and experiments. *Korean J. Chem. Eng.* **2021**, *38*, 1117–1128. [CrossRef]
46. Emeis, C.A. Determination of Integrated Molar Extinction Coefficients for Infrared Absorption Bands of Pyridine Adsorbed on Solid Acid Catalysts. *J. Catal.* **1993**, *141*, 347–354. [CrossRef]
47. Guo, Y.; Wang, S.; Geng, R.; Wang, P.; Li, S.; Dong, M.; Qin, Z.; Wang, J.; Fan, W. Enhancement of the dimethyl ether carbonylation activation via regulating acid sites distribution in FER zeolite framework. *iScience* **2023**, *26*, 107748. [CrossRef]
48. Xue, T.; Li, S.S.; Wu, H.H. Surfactant-promoted synthesis of hierarchical zeolite ferrierite nano-sheets. *Microporous Mesoporous Mater.* **2021**, *312*, 1107481–1107488. [CrossRef]
49. Xie, S.; Peng, J.; Xu, L.; Wu, Z.; Wang, Q. Synthesis of ZSM-35 zeolite using cyclohexylamine as organic template and its catalytic performance. *Chin. J. Catal.* **2003**, *24*, 531–534.
50. Houzvicka, J.; Nienhuis, J.G.; Ponec, V. The role of the acid strength of the catalysts in the skeletal isomerisation of *n*-Butene. *Appl. Catal. A Gen.* **1998**, *174*, 207–212. [CrossRef]
51. Xu, W.Q.; Yin, Y.G.; Suib, S.L.; Edwards, J.C.; O'Young, C.L. Modification of non-template synthesized ferrierite/ZSM-35 for n-Butene skeletal isomerization to isobutylene. *J. Catal.* **1996**, *163*, 232–244. [CrossRef]
52. Comelli, R.A. Skeletal Isomerization of Linear Butenes on Boron Promoted Ferrierite: Effect of the Catalyst Preparation Technique. *Catal. Lett.* **2008**, *122*, 302–309. [CrossRef]

Disclaimer/Publisher's Note: The statements, opinions and data contained in all publications are solely those of the individual author(s) and contributor(s) and not of MDPI and/or the editor(s). MDPI and/or the editor(s) disclaim responsibility for any injury to people or property resulting from any ideas, methods, instructions or products referred to in the content.